THE JOURNAL OF
PHYSICAL CHEMISTRY C

Article

Cite This: J. Phys. Chem. C 2017, 121, 26086-26095

pubs.acs.org/JPCC

A Hybrid Quantum-Classical Model of Electrostatics in Multiply Charged Quantum Dots

Hongbin Liu,[†] Carl K. Brozek,[†] Shichao Sun, David B. Lingerfelt, Daniel R. Gamelin,* and Xiaosong Li*

Department of Chemistry, University of Washington, Seattle, Washington 98195, United States

ABSTRACT: We present a general model for describing the properties of excess electrons in multiply charged quantum dots (QDs). Key factors governing Fermi-level energies and electron density distributions are investigated by treating carrier densities, charge compensation, and various material and dielectric medium properties as independently tunable parameters. Electronic interactions are described using a mean-field electrostatic potential calculable through Gauss's Law by treating the quantum dot as a sphere of uniform charge density. This classical approximation modifies the "Particle in a Sphere" Schrödinger equation for a square well potential and reproduces the broken degeneracy and Fermi-level energies expected from experiment and first-principles methods. Several important implications emerge from this model: (i) excess electron density drifts substantially toward the QD surfaces with high electron densities and large radii and when solvated by a high dielectric medium. (ii) The maximum density of the conduction-band electrons depends strongly on the dielectric strength of the solvent and the electron affinity and dielectric strength of the QD material. (iii) Fermi-level energies stabilize with charge-balancing cations in close proximity to the QD surface.

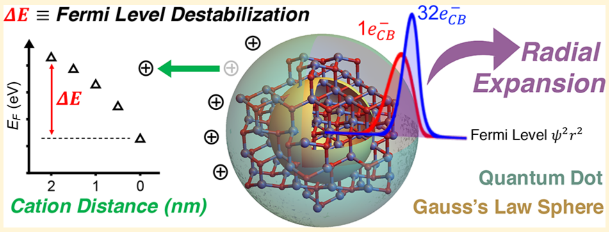

1. INTRODUCTION

The addition of excess charge carriers has emerged as a powerful tool for manipulating the physical and chemical properties of colloidal quantum dots (QDs). Multiple conduction-band (CB) electrons can be introduced synthetically through aliovalent doping or through electrochemical, thermochemical (remote chemical doping), or photochemical reduction (photodoping).[1] Charge mobilities, carrier dynamics, optical absorption, plasmon resonances, and various physical properties are altered upon charge accumulation. In certain materials, infrared plasmonics emerge that are tunable by charge, size, and composition,[2−4] giving rise to fascinating electrochromic[5] and magneto-optical behavior.[6] Electrostatic interactions between additional carriers and surface charges leads to dramatic shifts in band-edge potentials[7] and Stark-shifted luminescence.[8] At a fundamental level, many properties of excess electrons in charged QDs are not well understood, however. Despite progress in tuning carrier densities in various colloidal QD materials, such as ZnO, CdSe, PbS, InN, and In_2O_3,[9−13] the factors governing CB electron (e_{CB}^-) potentials and maximum achievable carrier densities remain largely unknown.

Mounting experimental evidence points to surface electrostatics as key determinants of QD band-edge potentials. Systematic modulation of PbS, HgS, and CdSe surface dipoles has been shown to tune their band-edge potentials by hundreds of mV.[7,14,15] Similar energetic shifts are observed by altering the ion-pairing strength of charged ZnO[16,17] QDs with charge-balancing cations of differing coordinating ability. Confinement and interelectronic interactions alone cannot account for these experimental observations. A convenient model is needed to describe excess electrons in charged QDs that accounts for electron−cation stabilization, dielectric effects, and interelectronic interactions. To the best of our knowledge, no such model exists.

The "Particle in a Sphere" model[18,19] is widely used to describe singly occupied QDs. Expressed in spherical coordinates, it solves the Schrödinger equation, $\hat{H}\Psi(r, \theta, \phi) = E\Psi(r, \theta, \phi)$. The potential $V(r)$ in the Hamiltonian is usually defined as a step function

$$V(r) = \begin{cases} -E_A, & r < R \\ 0, & r \geq R \end{cases} \tag{1}$$

where E_A is the electron affinity, and R is the radius of the QD. With the definition of $V(r)$ in eq 1, the solution of the single-electron Schrödinger equation is analytically tractable, with wave functions and energy levels taking the form

$$\Psi(r, \theta, \phi) = A\cdot\mathcal{R}_{nl}(r)\cdot Y_l^m(\theta, \phi) \tag{2}$$

$$E_{nl} = \frac{\beta_{nl}^2}{2R^2} \tag{3}$$

where $\mathcal{R}_{nl}(r)$ is the spherical Neumann function, $Y_l^m(\theta,\phi)$ is the spherical harmonic function, and A is a normalization constant. β_{nl} is the solution to the boundary condition of the spherical

Received: August 17, 2017
Revised: October 21, 2017
Published: October 23, 2017

ACS Publications

DOI: 10.1021/acs.jpcc.7b08224
J. Phys. Chem. C 2017, 121, 26086−26095

Neumann function. After the separation of variables (eq 2), an effective Hamiltonian, which is composed of kinetic, angular, and potential terms, can be written in atomic units for the radial function $\mathcal{R}(r)$ as

$$\hat{H}_r = -\frac{1}{2}\frac{d^2}{dr^2} + \frac{l(l+1)}{2r^2} + V(r) \tag{4}$$

This approach gives rise to hydrogenic orbitals, which have been reproduced using density functional theory (DFT) calculations of QD e^-_{CB}.[20] Whereas the square well potential assumed in eq 1 is sufficient for singly occupied QDs in the absence of surface chemistry, it does not describe interelectronic interactions of many-electron systems nor does it account for important experimental parameters such as charge compensation or the solvent dielectric strength. As electrons populate the CB, interelectronic and electron−countercation interactions significantly perturb the effective potential acting upon an e^-_{CB}. In first-principles methods, interelectronic interactions produce Coulomb and exchange contributions to the Fermi-level energy (E_F), but such calculations are only tractable for small clusters of atoms.[20−25] Here, we present a model of interelectronic and electron−cation interactions in multiply charged QDs that, through comparison with ab initio calculations and experimental results, accurately approximates E_F of charged QDs. By treating key experimental parameters as explicit variables in the model, their impact on the energetics of excess electrons can be investigated systematically for any QD material. We then illustrate how this versatile model can help explain emerging phenomena in multiply charged QDs.

2. RESULTS AND ANALYSIS

2.1. Theoretical Model.

The model presented here approximates interelectronic and electron−cation interactions by modifying the potential term of eq 4 to reflect a uniformly charged sphere. To distinguish our model from the "Particle in a Sphere" model with a square well potential, we term these the "Charged Sphere" and "Square Well" models, respectively. The "Charged Sphere" model consists of q^- number of electrons inside a spherical QD of radius R with q^+ compensating cations at the QD surface (Scheme 1). Employing Gauss's law, the effective potential outside the QD ($r \geq R$) arises from contributions from both q^+ and q^-

Scheme 1. Pictorial Representation of the "Charged Sphere" Model

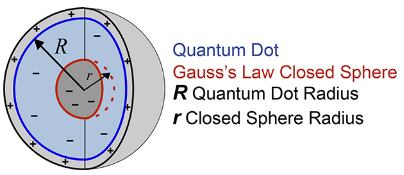

$$V^+(r) = -\frac{q^+}{\epsilon_{out} r},\ r \geq R;\ V^-(r) = +\frac{q^-}{\epsilon_{out} r},\ r \geq R \tag{5}$$

where ϵ_{out} is the dielectric constant of the medium (solvent or vacuum) surrounding the QD. In eqs 5−10, $V_{r=\infty}$ determines the zero reference.

q^+ and q^- make different contributions to the potential inside the QD ($r < R$). Because q^+ is distributed evenly across the QD surface, its contribution is equal everywhere inside the dot, and can be written as

$$V^+(r) = -\frac{q^+}{\epsilon_{out} R},\ r < R \tag{6}$$

The contribution of the electric field generated by q^- to the potential inside the QD ($r < R$) can be evaluated at any distance r using Gauss's Law (Scheme 1) as

$$E(r) = \frac{\iiint \rho(r)\,dV}{r^2 \epsilon_r},\ r < R \tag{7}$$

where ϵ_r and $\rho(r)$ are the dielectric constant and electron density inside the QD. As a starting point, the electron density and dielectric constant are uniform inside the QD, so that eq 7 can be rewritten as

$$E(r) = -\frac{q^- r}{\epsilon_R R^3} \tag{8}$$

where $\rho(r)$ is replaced by the homogeneous e^-_{CB} density (ρ^-_{CB}) inside the QD, $\rho^-_{CB} = \frac{q^-}{\left(\frac{4}{3}\pi R^3\right)}$, and the dielectric constant ϵ_r becomes the dielectric constant of the QD, ϵ_R. Integrating eq 8 from r to ∞ leads to the following expression for the potential inside the QD

$$V^-(r) = -\frac{q^- r^2}{2\epsilon_R R^3} + \frac{q^-}{2\epsilon_R R} + \frac{q^-}{\epsilon_{out} R},\ r < R \tag{9}$$

Combining eqs 1, 5, 6, and 9, the potential at any distance r can be expressed as

$$V(r) = \begin{cases} -\frac{1}{2\epsilon_R}[q^- r^2/R^3 - q^-/R] - \frac{1}{\epsilon_{out}}[(q^+ - q^-)/R + E_A] & r < R \\ -\frac{1}{\epsilon_{out}}[(q^+ - q^-)/r] & r \geq R \end{cases} \tag{10}$$

Figure 1 depicts the combined effect of the square well potential, a quantum mechanical property defined as E_A/ϵ_{out}, and the electrostatic contributions from q^+ and q^- to the total effective potential, $V(r)$. Varying q^- and q^+ in eq 10 leads to potentials with drastically different forms, as shown in Figure 1. Two scenarios are presented, $q^+ > 0$ and $q^+ = 0$, to illustrate the competing effects of $q^-/\epsilon_{out}R$ and $q^+/\epsilon_{out}R$ on the potential. Unless specified otherwise, discussion of the "Charged Sphere" model will refer to the scenario when $q^+ = q^-$. Below, this model is contrasted with the "Anionic Charged Sphere" ($q^+ = 0$) and the "Square Well" models to explore the impact of electron−cation and interelectronic interactions.

Eq10 suggests that for a given charged semiconductor QD surrounded by a dielectric medium (e.g., solvent), the potential depends on three tunable parameters: the size of the quantum dot (R), the excess electron density inside the QD ($\rho^-_{CB} \propto q^-$), and the density of surface counter cations ($\rho^+_{SUR} \propto q^+$). In the limit of large crystal radius ($R \to \infty$), it is easy to see from eq 10 that the potential inside the crystal approaches zero. On the other hand, in the limit of low ρ^-_{CB} ($q^- = 0$) and no surface counterions ($q^+ = 0$), the potential in eq 10 simply converges to the results from the "Square Well" model.

For QDs with multiple e^-_{CB}, the QD radius R strongly affects the shape of the potential inside the QD. Figure 2A plots $V(r)$ as a function of R for a ZnO QD solvated by tetrahydrofuran

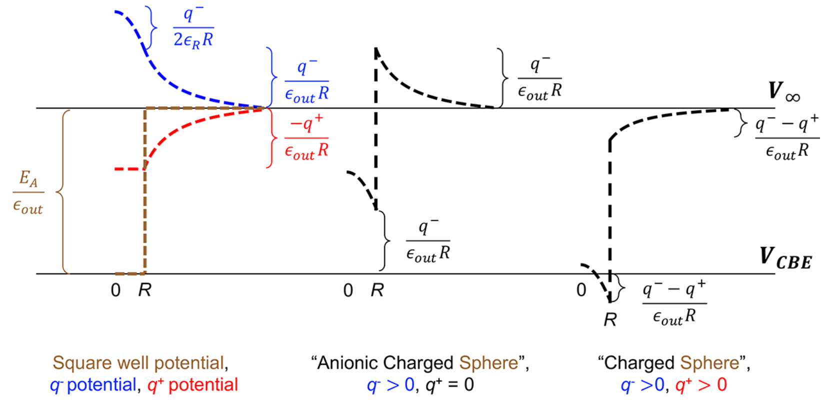

Figure 1. Illustration of the energetic contributions of the square well potential (brown), q^+ (red), and q^- (blue) to the total potential (black), with two specific scenarios highlighted: $q^- \neq 0$, $q^+ = 0$ (middle, "Anionic Charged Sphere" model) and $q^+ > 0$, $q^- > 0$ (right, "Charged Sphere" model). V_∞ and V_{CBE} denote the potential at $r = \infty$ and at the CB edge (CBE) of the undoped QD, respectively.

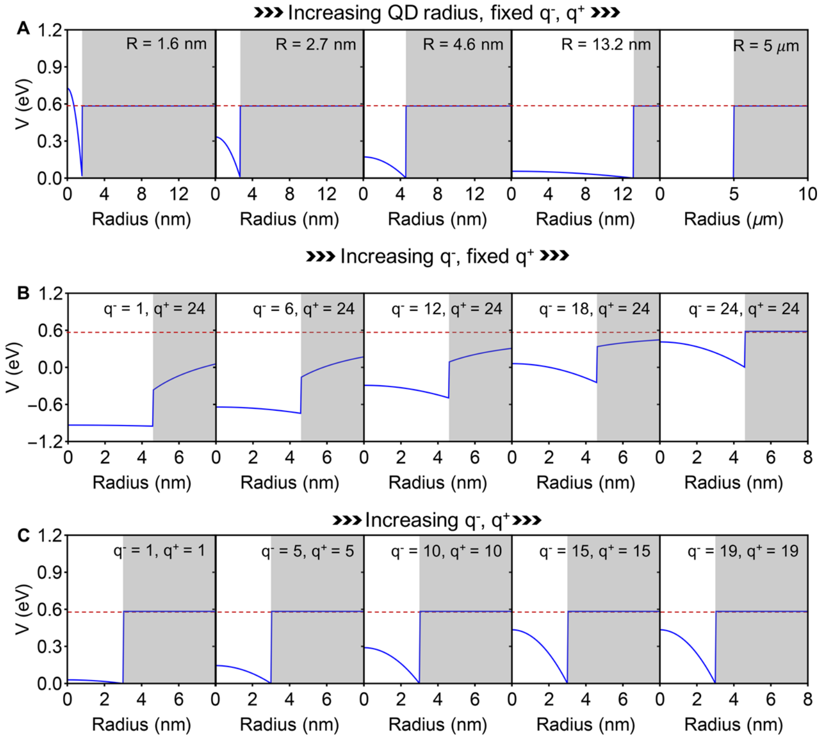

Figure 2. A: Size-dependence of the potential for a multiply charged ZnO QD with a fixed number of electrons solvated by THF ($q^- = q^+ = 10$). See eq 10 for the definition of $V(r)$. B: Electron density-dependence of the potential for a $R = 4.6$ nm ZnO QD solvated by THF with fixed $q^+ = 24$. C: Dependence of the potential on increasing numbers of q^+, q^- pairs in a $R = 3$ nm ZnO QD solvated by THF. ZnO and THF are simulated with $E_A = 4.2$ eV, $\epsilon_{out} = 7.56$. $r > R$ regions are shaded in gray. The horizontal red dashed line denotes the exterior potential bulk limit, E_A/ϵ_{out}. The zero reference is set at the V_{CBE} of pure undoped ZnO for all cases, i.e. $q^- = q^+ = 0$.

(THF) with $q^- = q^+ = 10$. Because evaluating $V(r)$ of undoped ZnO ($q^- = q^+ = 0$) requires an additional uncompensated probe electron, the same procedure was used to plot Figure 2. To compare against undoped ZnO, therefore, the zero reference was taken as the CB edge (CBE) of undoped ZnO. ZnO and THF are represented in the "Charged Sphere" model by choosing $E_A = 4.2$ eV and $\epsilon_{out} = 7.56$, respectively. When R is small, the prominent r^2 dependence of the potential inside the QD is consistent with classical Coulombic repulsion increasing for charges confined to a small volume. As the QD size increases, the potential inside the QD flattens, because the Coulombic repulsion is spread across a larger volume. The bulk limit is illustrated with an $R = 5$ μm sphere, where the charged sphere model yields the same results as the "Square Well" model. At the boundary ($r = R$), the potential is zero, because the contributions from both q^- and q^+ cancel exactly ($q^- = q^+$ for all examples shown in Figure 2A).

Figure 2B illustrates the effect of $\rho^-_{CB} \propto q^-$ on $V(r)$ when q^+ is fixed. Both E_A and ϵ_{out} are chosen again to simulate a ZnO QD solvated by THF. As the density increases, the interior potential rises, being highest at the origin and decreasing quadratically toward the surface. This behavior arises from interelectronic repulsion within the classical mean-field approximation. Figure 2B also illustrates that in accordance with eq 10, charge balancing cations (q^+: $q^- > 1$) lower both the interior and exterior potentials. This scenario is also depicted in the "Charged Sphere" model of Figure 1 and represents an extreme

DOI: 10.1021/acs.jpcc.7b08224
J. Phys. Chem. C 2017, 121, 26086−26095

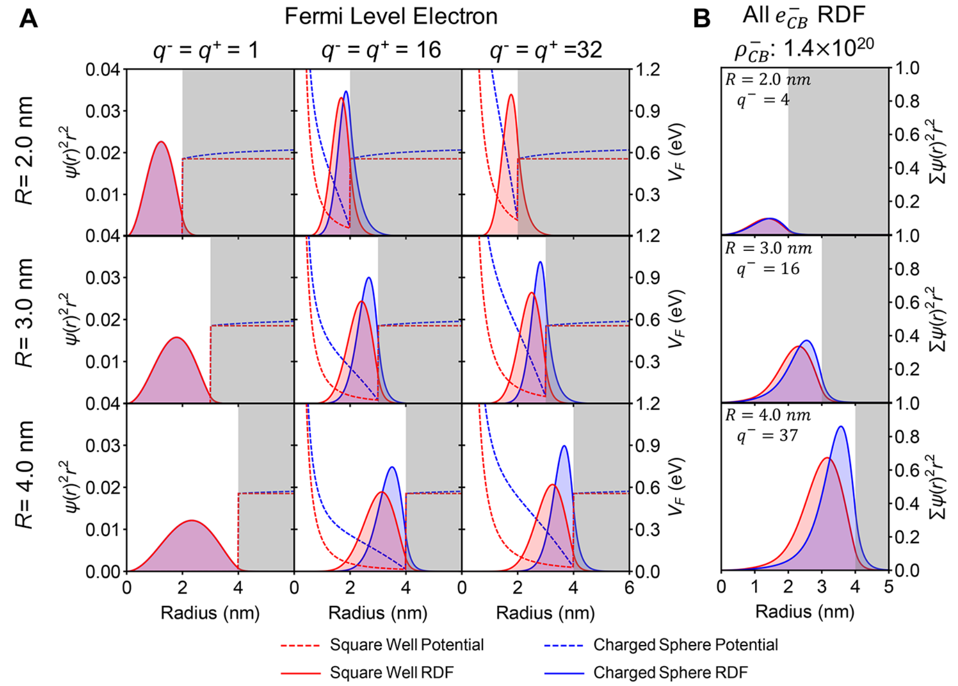

Figure 3. Comparison of the "Square Well" (red) and "Charged Sphere" (blue) models for a ZnO QD solvated by THF (E_A = 4.2 eV, ϵ_{out} = 7.56). The zero reference is set to the potential energy minimum for each QD size. A: Dependence of the potential energy of the Fermi-level electron (V_F) and radial-distribution functions ($\psi(r)^2r^2$) of the QD Fermi-level electron on the QD radius (R) and number of q^-, q^+ pairs. Potentials are plotted as dashed lines, and $\psi(r)^2r^2$ are plotted as shaded curves. B: Dependence of the sum-total $\psi(r)^2r^2$ of all e^-_{CB} ($\Sigma\psi(r)^2r^2$) on R at a fixed ρ^-_{CB}.

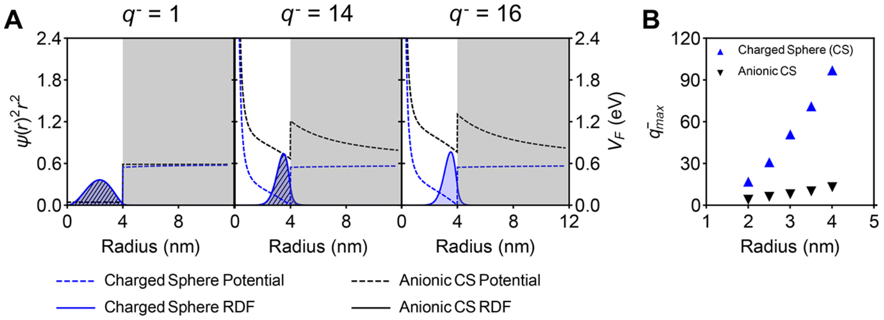

Figure 4. Comparison of the "Charged Sphere" (blue) and "Anionic Charged Sphere" (black) models for an R = 4 nm ZnO QD solvated by THF (E_A = 4.2 eV, ϵ_{out} = 7.56). A: Dependence of V_F and $\psi(r)^2r^2$ of the QD Fermi-level electron on the QD radius, R, and number of q^-, q^+ pairs. Potentials are plotted as dashed lines, and $\psi(r)^2r^2$ are plotted as shaded curves (hashed black for the "Anionic Charged Sphere" model). V_F of the "Anionic Charged Sphere" model are baseline corrected so that the zero reference is taken as the minimum potential of the "Charged Sphere" model. B: Size-dependence of q^-_{max}.

limit of charged QDs with large electrical double layers due to low electrolyte concentrations.

Figure 2C depicts the scenario where overall charge neutrality is maintained at the surface of an R = 3 nm ZnO QD solvated by THF. For different values of $q^+ = q^-$, the exterior potential remains constant, whereas the interior potential rises sharply with electron accumulation. The maximum number of e^-_{CB} (q^-_{max}) that can be stabilized in a QD is given by the value where E_F equals the exterior potential energy. Because $q^- = q^+$, the potential again equals zero at the QD surface, where both contributions cancel exactly.

The results presented above illustrate the impact of QD size and charge density on the energetics of excess CB electrons in QDs. As seen from Figure 2A−C, in the case of weak interelectronic repulsion or bulk-like crystal sizes, the "Square Well" model is sufficient, but this model fails when multiple excess electrons are confined to small volumes, which is the scenario of most interest when studying charged QDs.

2.2. Implementation of the "Charged Sphere" Model.

Whereas analytical solutions of the Schrödinger equation using the "Square Well" model (eq 1) can be obtained (eqs 2 and 3), the Schrödinger equation using the "Charged Sphere" model (eq 10) does not have analytical solutions. Instead, the discrete variable representation (DVR) approach[25,26] is used to numerically solve the Schrödinger equation for e^-_{CB}, with the potential as defined in eq 10. To compare eqs 5−10 and Figure 2 against undoped ZnO ($q^- = q^+ = 0$), an additional uncompensated probe electron was used to evaluate $V(r)$. As a result, the potential at $r = R$ equals zero, because the interactions of q^- and q^+ with the probe electron are equal and opposite. This potential is identical to the CB edge (V_{CBE}) of undoped ZnO ($q^- = q^+ = 0$) and is therefore the zero reference in Figure 2. All other calculations with the "Charged Sphere" model treat the nth electron as a probe of the mean field created by the previous $n - 1$ electrons so that the minimum potential, always at $r = R$, lies $-1/\epsilon_{out}R$ lower than the V_{CBE} of the corresponding undoped ZnO QD due to stabilization by q^+, in accordance with eq 10 and as depicted by Figure 1. Consequently, the zero reference for these calculations, and in Figures 3, 6, 7, and 8, is taken as the minimum value for convenience. The zero reference of Figure 4 is taken as the minimum of the "Charged Sphere" model, which lies $q^-/\epsilon_{out}R$ below the minimum of the "Anionic Charged Sphere" model. As stated previously, we solve the radial part of the Schrödinger equation for a given angular momentum. The size-dependent dielectric constant formalism[27]

$$\epsilon_R = 1 + \frac{\epsilon_0 - 1}{1 + \frac{1.8}{R^{1.7}}} \tag{11}$$

is used throughout the paper, where ϵ_0 is the static dielectric constant.

2.3. Comparison to the "Square Well" Model.

Figure 3 compares the potential energies of the Fermi-level electron (V_F) and radial-distribution functions ($\psi(r)^2r^2$) calculated from both the "Charged Sphere" and "Square Well" models for different R and ρ_{CB}^-. Both models incorporate the centrifugal potential $\frac{l(l+1)}{2r^2}$ arising from orbital angular momentum. At low ρ_{CB}^-, the solutions of the two models are nearly identical for all sizes. As ρ_{CB}^- increases at a fixed QD size, however, the solutions of the "Square Well" and the "Charged Sphere" models begin to deviate. Both models predict a shift of the radial-distribution function toward the surface at higher angular momentum due to the centrifugal potential. This shift causes a large degree of e_{CB}^- tunneling ("spill out"). Compared with the "Square Well" solutions, the e_{CB}^- in the "Charged Sphere" model shift more toward the QD surface because of interelectronic repulsion, resulting in a narrower distribution (Figure 3). For example, in the case of $q^- = q^+ = 32$ in an $R = 4.0$ nm QD, the difference between the positions of the distribution maxima is as large as 0.41 nm, with a full-width-at-half-maximum (fwhm) difference of 0.43 nm. The right hand side of Figure 3 shows that for a fixed electron density, this deviation is accentuated with increasing R. For example, when $\rho_{CB}^- = 1.4 \times 10^{20}$ cm^{-3} in an $R = 4.0$ nm QD, the sum total $\psi(r)^2r^2$ of all e_{CB}^- ($\Sigma\psi(r)^2r^2$) from the "Square Well" model resides at $r = 3.17$ nm with a 1.35 nm fwhm, whereas the "Charged Sphere" model predicts a maximum at $r = 3.58$ nm with a 0.99 nm fwhm. At this ρ_{CB}^- and $R = 2.0$ nm, the "Square Well" and the "Charged Sphere" models produce nearly identical results.

2.4. Comparison to the "Anionic Charged Sphere" Model.

To evaluate the energetic stabilization provided by charge-balancing cations, we compare V_F in the "Anionic Charged Sphere" and "Charged Sphere" models. From Figure 1, the interior potential in the "Anionic Charged Sphere" model raises by $q^-/\epsilon_{out}R$ above V_{CBE}, where q^- is the number of uncompensated e_{CB}^-, consequently also shifting the E_F by $q^-/\epsilon_{out}R$. This Coulombic term suggests charge-balancing cations provide the greatest stabilization for highly charged QDs with a small R and ϵ_{out}.

Figure 4 compares V_F and $\psi(r)^2r^2$ calculated from the "Charged Sphere" ($q^+ = q^-$, blue) and "Anionic Charged Sphere" ($q^+ = 0$, black) models for an $R = 4$ nm ZnO QD solvated by THF ($E_A = 4.2$ eV, $\epsilon_{out} = 7.56$) for several values of q^-. The left hand figure shows that $\psi(r)^2r^2$ (shaded curves) calculated from both models are nearly identical when $q^- < 16$. The calculated potentials (dashed lines) on the other hand deviate even at $q^- = 1$, with the "Anionic Charged Sphere" model predicting higher E_F. At $q^- = 16$, the interior potential rises above the exterior potential, causing the maximum of $\psi(r)^2r^2$ to lie outside the QD. In other words, QDs with uncompensated e_{CB}^- support lower electron densities. The right hand panel of Figure 4 summarizes this result across QD sizes, showing again that modeling charged QDs without surface cations ($q^+ = 0$) systematically underestimates q_{max}^-.

2.5. Comparison to DFT and Experiment.

To evaluate the accuracy of the "Charged Sphere" model, we compared its solutions to DFT calculations of small QDs. Details of the DFT calculations are provided in the Methods section. Figure 5 compares E_F from the "Charged Sphere", "Anionic Charged Sphere", and "Square Well" models with DFT calculations of $Zn_{33}O_{33}$ ($R = 0.6$ nm), $Zn_{84}O_{84}$ ($R = 0.7$ nm), and $Zn_{153}O_{153}$ ($R = 0.8$ nm) as well as experimental results[9,16] of various ZnO QDs. Figure 5A plots the predicted energetic difference between the 1 e_{CB}^- and 2 e_{CB}^- Fermi levels (ΔE_F) of $R = 0.6$ nm, $R = 0.7$ nm, and $R = 0.8$ nm ZnO QDs in vacuum ($\epsilon_0 = 1$). The "Square Well" model predicts degeneracy of these levels

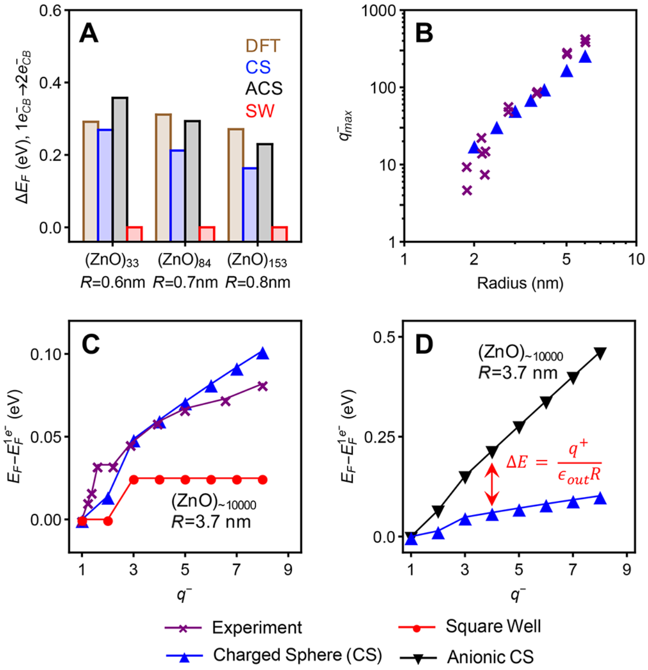

Figure 5. Comparison of ZnO QD Fermi-level energies (E_F) calculated using the "Square Well", "Charged Sphere", and "Anionic Charged Sphere" models ($E_A = 4.2$ eV, $\epsilon_{out} = 1$ (vacuum)) with DFT and experimental results.[16] A: Energetic difference (ΔE_F) between 1 e_{CB}^- and 2 e_{CB}^- Fermi levels of $R = 0.6$ nm, $R = 0.7$ nm, and $R = 0.8$ nm ZnO QDs calculated from the "Square Well", "Charged Sphere", "Anionic Charged Sphere" models, and DFT. B: Comparison of the maximum number of e_{CB}^- (q_{max}^-) from experiments given in ref 9 and calculated by the "Charged Sphere" model. C: Comparison of calculated relative E_F values with experimental results for THF-solvated $R = 3.7$ nm ZnO QDs. Energies are plotted relative to the E_F at $1e_{CB}^-$ ($E_F^{1e^-}$). D: Comparison of E_F values calculated from the "Charged Sphere" and "Anionic Charged Sphere" models. The difference is equal to the term written in red. The baseline is corrected so that the zero reference is set at the minimum value calculated from the "Charged Sphere" model.

DOI: 10.1021/acs.jpcc.7b08224
J. Phys. Chem. C 2017, 121, 26086−26095

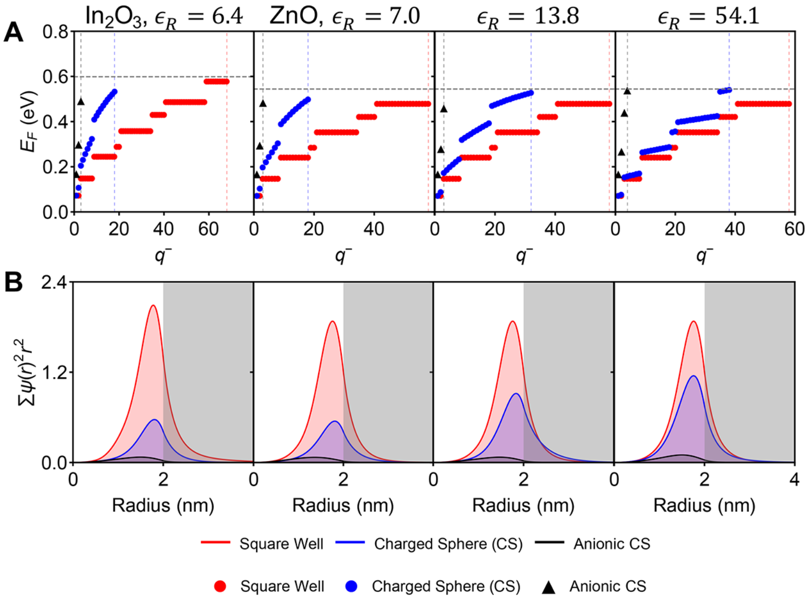

Figure 6. Comparison of E_F (A) and $\Sigma\psi(r)^2r^2$ (B) and of R = 2 nm ZnO, In$_2$O$_3$, and two hypothetical QDs using the "Square Well", "Charged Sphere", and "Anionic Charged Sphere" models. A: E_F of QDs with increasing e^-_{CB} accumulation. Horizontal lines indicate the E_A/ϵ_{out} of each material. Vertical lines denote q^-_{max} according to each color-coded model. B: Comparison of $\Sigma\psi(r)^2r^2$ of the same series of QDs at the predicted q^-_{max} of each. ϵ_R was calculated from eq 11, using ϵ_0 values of 9, 10, 20, and 80 for In$_2$O$_3$, ZnO, and the two hypothetical materials, respectively.

(ΔE_F = 0), whereas the "Charged Sphere" and "Anionic Charged Sphere" models and DFT calculate nonzero ΔE_F values that are numerically similar to average values of ΔE_F = 0.31, 0.25, and 0.20 eV for the R = 0.6, 0.7, and 0.8 nm QDs, respectively.

For comparison against two key experimental signatures of multiply charged QDs, the "Charged Sphere" model was used to compute the size dependence of q^-_{max} and the impact of many additional charge carriers on E_F. Figure 5B compares q^-_{max} determined from the "Charged Sphere" model with experimental results of ZnO QDs photodoped in the presence of Li[HBEt$_3$] or K[HBEt$_3$].[9] Excellent numerical agreement between theory and experiment show increasing q^-_{max} for larger QD sizes. The strong size dependence of q^-_{max} observed experimentally for ZnO,[9] In$_2$O$_3$, Sn/In$_2$O$_3$,[13] and InN[12] QDs can therefore be interpreted in terms of the "Charged Sphere" model, as large QDs requiring greater numbers of excess charges to reach the destabilizing interior effective potential that limits q^-_{max}. Figure 5C compares E_F values of THF-solvated R = 3.7 nm ZnO QDs from experiment and predicted by the "Square Well" and "Charged Sphere" models. For clarity, the zero reference in this figure is taken as E_F at 1e^-_{CB} ($E_F^{1e^-}$) rather than V_{CBE} because the "Charged Sphere" model predicts this value to lie nearly $\frac{1}{\epsilon_{out}R}$ below V_{CBE}, leading to an nonphysical negative value. Note that we are unable to calculate the electronic structure of an R = 3.7 nm ZnO QD using DFT due to computational expense. The solutions to the "Square Well" model are a set of hydrogenic orbitals with degeneracy within each orbital shell (S, P, D, ...). By excluding interelectron repulsion, these orbitals fill in a staircase fashion with constant potential for each orbital shell. In contrast, the "Charged Sphere" model reproduces the more gradual increase in E_F observed in experiment[16] and that expected for multielectron systems when interelectronic repulsion is included.

Figure 5D illustrates that the "Anionic Charged Sphere" model calculates E_F values that are systematically raised by $q^-/\epsilon_{out}R$ after applying the baseline correction described above. Even at low e^-_{CB} accumulation, a lack of charge compensation destabilizes E_F by hundreds of meV.

2.6. Comparison of Different QD Materials.

Figure 6 compares $\Sigma\psi(r)^2r^2$ and E_F for R = 2 nm In$_2$O$_3$ and ZnO QDs solvated by THF (ϵ_{out} = 7.56), simulated using E_A values of 4.45 and 4.2 eV[28,29] and ϵ_0 of 9 and 10, respectively. Two hypothetical materials were also included to illustrate the impact of ϵ_0 by setting ϵ_0 = 20 and ϵ_0 = 80 but keeping the E_A of ZnO. For each material, ϵ_R was calculated from ϵ_0 using eq 11. Figure 6A compares E_F computed from the "Square Well", "Charged Sphere", and "Anionic Charged Sphere" models vs number of e^-_{CB}. Horizontal lines indicate E_A/ϵ_{out} and vertical lines denote the q^-_{max} according to each color-coded model. Figure 6B compares the $\Sigma\psi(r)^2r^2$ of the QD materials at q^-_{max}, determined for all models as when the highest bound E_F is reached, i.e., when $E_F = E_A/\epsilon_{out}$.

Figure 6 illustrates the impacts of ϵ_R and E_A in the "Charged Sphere" model on E_F, and, hence, q^-_{max} of a QD material. As suggested by eq 9, a large ϵ_R screens the interior potential and interelectronic repulsion. As a result, for similar values of E_A, higher dielectric materials accumulate more e^-_{CB} and exhibit diminished orbital energy splitting within a given orbital shell. A larger E_A, on the other hand, imposes a higher tunneling barrier, allowing more e^-_{CB} to accumulate. Therefore, despite In$_2$O$_3$ having ϵ_R smaller than ZnO, its larger E_A results in the two materials having similar q^-_{max}. As discussed above, the "Anionic Charged Sphere" model predicts Fermi-level energies that are greatly destabilized relative to the "Charged Sphere" results, and fewer e^-_{CB} accumulate in each material, resulting in the smallest q^-_{max} in Figure 6A and $\Sigma\psi(r)^2r^2$ in Figure 6B. The "Square Well" model, in contrast, predicts much higher q^-_{max} as a consequence of neglecting interelectronic repulsion and fails to reproduce the constant increase in E_F with increasing values of q^-.

2.7. Solvation Effects.

Solvation effects can be simulated within the "Charged Sphere" model by adjusting ϵ_{out}. Figure 7

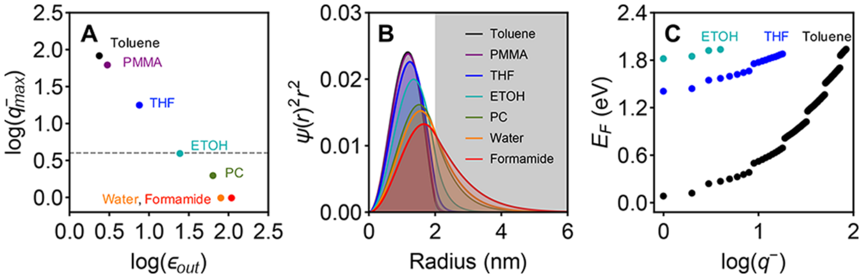

Figure 7. Solvent dependence of the $e^-_{CB_{max}}$ (A), 1-e^-_{CB} $\Sigma\psi(r)^2r^2$ (B), and E_F (C) for $R = 2$ nm ZnO QDs using the "Charged Sphere" model, simulated by varying ϵ_{out}. The Fermi-level zero reference is set to the potential minimum for the QD solvated by toluene. The horizontal dashed line in the leftmost panel denotes the experimentally determined q^-_{max} for colloidal ZnO QDs. Solvent ϵ_{out} was adjusted as follows: toluene ($\epsilon_0 = 2.38$), poly(methyl methacrylate) (PMMA, $\epsilon_0 = 3$), THF ($\epsilon_0 = 7.56$), ethanol (EtOH, $\epsilon_0 = 24.5$), propylene carbonate (PC, $\epsilon_0 = 64$), water ($\epsilon_0 = 80.1$), and formamide ($\epsilon_0 = 111$).

plots q^-_{max}, $\Sigma\psi(r)^2r^2$, and E_F for an $R = 2$ nm ZnO QD in various dielectric media chosen for their experimental relevance: toluene ($\epsilon_0 = 2.38$), poly(methyl methacrylate) (PMMA, $\epsilon_0 = 3$), THF ($\epsilon_0 = 7.56$), ethanol (EtOH, $\epsilon_0 = 24.5$), propylene carbonate (PC, $\epsilon_0 = 64$), water ($\epsilon_0 = 80.1$), and formamide ($\epsilon_0 = 111$). As suggested by eq 5, ϵ_{out} screens E_A, lowering the tunneling barrier and decreasing the q^-_{max}. The leftmost panel of Figure 7 compares q^-_{max} as a function of ϵ_{out}. The smallest ϵ_{out} leads to greatest e^-_{CB} accumulation by maximizing the barrier height E_A/ϵ_{out}. The middle panel of Figure 7 illustrates the impact of ϵ_{out} on $\psi(r)^2r^2$ at a fixed q^-_{max}. In the 1-e^-_{CB} limit, the $\Sigma\psi(r)^2r^2$ expands toward the QD surface with increasing ϵ_{out}. The rightmost panel of Figure 7 plots E_F for three selected solvents vs log of e^-_{CB}, illustrating that weaker dielectric solvents lower the interior QD potential, decrease E_F, and greatly confine $\psi(r)^2r^2$.

2.8. Surface Proximity of Charge-Balancing Cations.

The dependence of E_F on the distance (ΔR) of charge-balancing cations from QD surfaces was also examined within the "Charged Sphere" model. E_F increases as q^+ moves away from the QD surface, as illustrated in the left-hand-side of Figure 8. To calculate the Coulombic destabilization of displacing charge-balancing cations from the QD surface, an energetic correction of $\frac{q^+}{\epsilon_{out}R} - \frac{q^+}{\epsilon_{out}(R + \Delta R)}$ is added to E_F.

The right panel of Figure 8 plots E_F of a ZnO QD in the $q^- = q^+ = 1$ limit vs ΔR for a variety of R and ϵ_{out}. $\Delta R = 2$ nm is the largest distance considered. This distance coincides with the approximate length of a typical surface-capping ligand such as trioctylphosphonate. In all cases, displacement of the cations from the QD surfaces leads to destabilization of E_F. Comparing E_F for $R = 4$ nm vs $R = 2$ nm ZnO QDs solvated by THF shows that smaller QDs experience greater Coulombic destabilization. Comparing $R = 2$ nm ZnO QDs solvated by THF ($\epsilon_0 = 7.56$) vs toluene ($\epsilon_0 = 2.38$), on the other hand, illustrates that QDs in weaker dielectric media are more sensitive to cation displacement. Although these results were obtained for $q^- = q^+ = 1$, the correction term scales linearly with q^+, and so, similar trends are predicted for other values of q^+ and q^-.

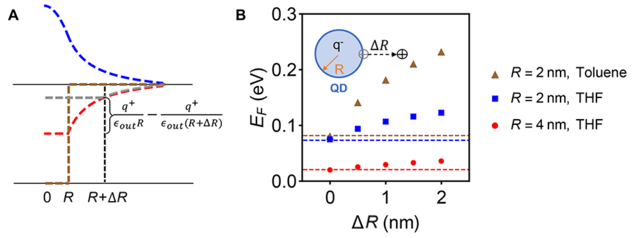

Figure 8. A: The potential difference resulting from q^+ displacement from the QD surface. Contributions from E_A/ϵ_{out}, q^-, q^+ at R, and q^+ at $R + \Delta R$ are shown in brown, blue, red, and gray, respectively. B: Dependence of E_F calculated from the "Charged Sphere" model on the surface proximity of charge-balancing cations (ΔR) for a ZnO QD (E_A = 4.2 eV) with $q^- = q^+ = 1$ and varying R and solvent media (ϵ_{out}). Horizontal lines denote the energy at $\Delta R = 0$ for comparison.

3. METHODS

3.1. DFT Calculations.

All electronic structure calculations were performed using the development version of the Gaussian program.[30] Nearly spherical wurtzite phase ZnO QDs having C_{3v} symmetry were built according to the previously published scheme[31,32] using lattice parameters from the American Crystal Structure Database. The coordinatively unsaturated surface atoms were passivated using pseudohydrogen atoms with modified nuclear charges of +0.5 and +1.5 to terminate surface O^{2-} and Zn^{2+} ions, respectively, for neutral QDs.[31,32] In the case of QDs charged with e^-_{CB}, this pseudohydrogen capping scheme also allows us to create a homogeneous distribution of surface compensating charges by increasing the nuclear charge of each pseudohydrogen by δ^+ so that $q^+ = \sum\delta^+$. A uniform distribution of fractional charges simulates the realistic scenario of dipoles induced by localized cations and delocalized electrons being counterbalanced by large numbers of other dipoles distributed over the entire QD surface. The PBE0 hybrid DFT functional was used[33−35] along with the Los Alamos double-ζ pseudopotential and the associated valence double-ζ basis (LANL2DZ) for the lattice.[36−38] This methodology has already shown promising results for the theoretical characterization of diluted magnetic semiconductors, e.g., doped ZnO QDs, and for charged ZnO QDs in the limit of one excess electron.[20,32,39−43] All DFT calculations were performed in vacuum.

3.2. Model Calculations.

The discrete variable representation (DVR) approach[25,26] is used to numerically solve the Schrödinger equations in the hybrid model. The DVR code is implemented in Python and is publicly available.[44] A fine grid composed of 1000 Gauss-Hermite quadrature points was employed in the DVR calculations. The eigenfunction and corresponding radial-distribution function were collected with 0.02 nm resolution.

4. DISCUSSION

The "Charged Sphere" model presented above offers four key predictions about excess electron accumulation in colloidal QDs: (i) $\psi(r)^2r^2$ dramatically shifts toward the QD surfaces with larger ϵ_{out}, R, or ρ^-_{CB}. (ii) For a fixed dielectric medium, QDs with larger values of E_A and ϵ_r can sustain higher $\rho^-_{CB_{max}}(\propto q^-_{max})$ values. (iii) Weaker dielectric media promote greater $\rho^-_{CB_{max}}$ by increasing the barrier height for electron escape. (iv) Charge-balancing cations closer to the QD surfaces stabilize e^-_{CB} more effectively.

Although the "Charged Sphere" model uses a uniform charge density to construct the interior potential, a key insight is that excess electrons in highly charged QDs shift toward the QD surfaces. The resulting electron density distributions are reminiscent of Schockley or Tamm delocalized surface states.[45] Our analysis suggests that these states become more relevant in larger QDs with greater ρ^-_{CB}.

The "Charged Sphere" model helps explain several experimental observations. For example, the model correctly predicts similar $\rho^-_{CB_{max}}$ in colloidal In_2O_3 and ZnO QDs, determined from experiment to be 2.3×10^{20} cm^{-3} and 1.4×10^{20} cm^{-3}, respectively.[9,13] Numerically, the model predicts $\rho^-_{CB_{max}}$ of 5.4×10^{20} cm^{-3} for both materials when photodoped in the presence of EtOH. A likely explanation for this higher predicted $\rho^-_{CB_{max}}$ is that the model neglects competing redox transformations such as QD oxidation reactive surface species. As E_F rises with greater ρ^-_{CB}, these processes may dominate. In line with this reasoning, acetaldehyde hydrogenation was invoked previously as introducing a limit to $\rho^-_{CB_{max}}$ in colloidal ZnO QDs photodoped using EtOH as the hole quencher.[16] Interestingly, photodoping ZnO QDs with Li[$HBEt_3$], thereby eliminating formation of acetaldehyde, leads to higher $\rho^-_{CB_{max}}$ of 6×10^{20} cm^{-3}, much more similar to our predicted value. This model, therefore, estimates an upper limit of $\rho^-_{CB_{max}}$ for a QD material in the absence of competing redox processes.

The strong size dependence of q^-_{max} for a given QD material is accurately predicted by the "Charged Sphere" model. Agreement between experiment and calculations in Figure 5B provides a basis for understanding why larger ZnO,[9] In_2O_3, Sn/In_2O_3,[13] and InN[12] QDs accumulate greater q^-_{max} and display volume-independent $\rho^-_{CB_{max}}$ regardless of whether charges arrive through photodoping, remote chemical doping, or reductive synthetic conditions. Electrons accumulate in QDs until the interior effective potential rises above a threshold value that causes spontaneous charge ejection. Whereas the "Charged Sphere" model simulates this process as QD ionization into solvated electrons and cationic QDs, reports have postulated Zn(0) metal formation in the case of ZnO QD photodoping, for instance.[9] Despite mechanistic differences of charge ejection between experiment and theoretical predictions, the "Charged Sphere" model captures the essence of the strong size dependence of q^-_{max} with remarkable numerical accuracy.

Solvent dependencies of $\rho^-_{CB_{max}}$ are also explainable by the "Charged Sphere" model. A previous study of electrochemical electron injection into a thin-film assembly of $R = 2.15$ ZnO QDs reported a solvent dependence consistent with the one predicted by the "Charged Sphere" model (Figure 7).[46] Electron injection in EtOH, PC, and water led to q^-_{max} values of 4, 2, and 11, respectively, compared to predicted values of 4, 2, and 1 for $R = 2$ ZnO QDs. Interestingly, the ϵ_0 of water at the surface of an electrode is known to be at least ten times smaller than its bulk value,[47] which would bring the calculated q^-_{max} for this solvent in line with experiment. The q^-_{max} values predicted by the "Charged Sphere" model for ZnO QDs in toluene, PMMA, and THF are not observed experimentally, however. Lower values of q^-_{max} are observed likely because of competing redox processes, such as charge trapping at surfaces. For example, the high calculated values of q^-_{max} may not be achievable in weak dielectric media because these solvents poorly solubilize cations, leading to ineffective charge compensation at the QD surface and higher E_F. The general agreement with experiments performed in EtOH, PC, and water suggest that among sufficiently strong dielectric media, the key determinant of $\rho^-_{CB_{max}}$ is the ability of the dielectric to screen the QD E_A and stabilize e^-_{CB}. Again, the "Charged Sphere" model estimates an upper limit of $\rho^-_{CB_{max}}$ achievable in a given dielectric medium.

The higher E_F calculated for QDs with q^+ displaced from the surface supports experimental observations that surface electrostatics greatly impact e^-_{CB} stabilization.[7,14−17,48] Altering ΔR simulates the effect of poor ion-pairing and low electrolyte concentrations at the QD surface, with the "Anionic Charged Sphere" model representing an extreme limit of cation displacement. Consistent with experimental evidence, Figure 8 predicts these electrostatic factors to impact E_F by hundreds of meV. For example, one report has shown that $R = 1.9$ nm ZnO colloidal QDs in toluene charged to the 1-e^-_{CB} limit are destabilized by 600 mV when compensated by $[CoCp^*_2]^+$ vs H^+.[16] For comparison, the maximum destabilization obtained by displacing cations from the surface of an $R = 1.9$ nm QD solvated by toluene is predicted to be 320 meV (by setting $\Delta R = \infty$). The precise value depends heavily on ϵ_{out}, which likely differs from ϵ_0 of the bulk solvent, because the QD surface is surrounded by ligands and other chemical species, in addition to solvent. Reducing ϵ_{out} by half would reproduce the 600 mV destabilization and is reasonable given solvent exclusion from the QD ligand shell and the weak dielectric ligands used.

Adjusting ΔR can also be used simulate experimental observations that q^-_{max} depends on the electrolyte concentration and composition of the electrical double layer. For example, E_F of Se^{2-}-rich $R = 2.7$ nm CdSe colloidal QDs has been demonstrated experimentally to stabilize by over 250 mV simply by increasing the concentration of the $[Bu_4N][PF_6]$ electrolyte, thereby decreasing the length of the electrical double layer and improving charge-compensation at the QD surface. This value is similar to the 224 meV maximum destabilization energy predicted for $R = 2.7$ nm ZnO QDs in toluene (Figure 8). A dependence of E_F on the proximity of charge-balancing cations has also been reported in potentiometric titrations of multiply charged ZnO QDs.[17] Displacing charge-balancing protons from the surfaces of charged ZnO QDs with increasing amounts of bulky noncoordinating diammonium ions leads to systematic destabilization of E_F without changing the number of e^-_{CB}.

Conceptually, the "Charged Sphere" model relates to the classical electrostatic expression $\Delta V = \mu N/\epsilon_0$ invoked previously to calculate the shift ΔV of QD band-edge potentials resulting from a surface density N of dipoles with magnitude μ.[7,15,48] Both predict a shift of E_F when the QD surface is surrounded by separated point charges screened by a dielectric medium. Whereas the expression above treats this charge separation specifically as a dipole with quantifiable strength μ, the "Charged Sphere" model parametrizes this interaction more generally as q^- separated from q^+ by ΔR, allowing a greater variety of surface phenomena to be modeled, such as dependence on electrolyte concentration and coordinating strength of the countercation. Further development of the "Charged Sphere" model will allow more detailed description of specific aspects of the electrical double layer, but these results already provide valuable insight into the electrostatics of QD surfaces.

The accuracy of the "Charged Sphere" model can be improved through several modifications. First, the Schrödinger equation can be solved iteratively by proceeding from $V(r)$ determined through Gauss's Law using the previously calculated electron density. Also, introducing additional parameters to model the electrical double layer and modifying E_A as a function of electron doping level would improve both E_F and $\psi(r)^2r^2$. The model presented here was chosen to balance convenience and accuracy.

5. CONCLUSION

In summary, we present a quantum model for describing E_F and $\psi(r)^2r^2$ of excess electrons in multiply charged QDs. This "Charged Sphere" model successfully accounts for interelectronic and electron−cation interactions using classical electrostatics and exhibits marked quantitative advantages over models that neglect charge-compensating cations at the QD surfaces or interelectronic interactions. The model is generalizable to many materials and dielectric media by using the adjustable parameters ϵ_R, ϵ_{out}, and E_A. Its predictions agree well with both DFT and experiment. The model's predictions of an expansion of excess electron density toward the QD surfaces and a strong dependence of E_F on the proximity of charge-balancing cations provide a theoretical basis for understanding and quantifying the sensitivity of multiply charged QDs to surface chemistry. Future work will focus on extending this model to p-type semiconductor QDs with excess holes, to aliovalently doped QDs, and to modeling electrical double layers. Beyond providing insights into the characteristics of multiply charged QDs as discussed above, the quantitative description of key experimental factors determining V_{CBE} outlined here will help guide the understanding of surface electrostatic effects on QD electron-transfer processes including those involved in QD-based photovoltaics, solar photocatalysis, and electrical devices.

■ AUTHOR INFORMATION

Corresponding Authors

*E-mail: gamelin@chem.washington.edu (D.R.G.)
*E-mail: xsli@uw.edu (X.L.)

ORCID

Hongbin Liu: 0000-0001-9011-1182
Shichao Sun: 0000-0002-7680-3972
Daniel R. Gamelin: 0000-0003-2888-9916
Xiaosong Li: 0000-0001-7341-6240

Author Contributions

[†]H.L. and C.K.B. contributed equally

Notes

The authors declare no competing financial interest.

■ ACKNOWLEDGMENTS

The development of the computational model is supported by the NSF (CHE-1464497 to X.L., CHE-1506014 to D.R.G., and DMR-1719797). The development of open-source computational code is supported by the NSF Office of Advanced Cyberinfrastructure (OAC-1663636 to X.L.). This work was facilitated though the use of advanced computational, storage, and networking infrastructure provided by the Hyak supercomputer system and was funded by the STF at the University of Washington and the National Science Foundation (MRI-1624430).

■ REFERENCES

(1) Schimpf, A. M.; Knowles, K. E.; Carroll, G. M.; Gamelin, D. R. Electronic Doping and Redox-Potential Tuning in Colloidal Semiconductor Nanocrystals. *Acc. Chem. Res.* **2015**, *48*, 1929−1937.

(2) Kriegel, I.; Scotognella, F.; Manna, L. Plasmonic Doped Semiconductor Nanocrystals: Properties, Fabrication, Applications and Perspectives. *Phys. Rep.* **2017**, *674*, 1−52.

(3) Comin, A.; Manna, L. New Materials for Tunable Plasmonic Colloidal Nanocrystals. *Chem. Soc. Rev.* **2014**, *43*, 3957−3975.

(4) Schimpf, A. M.; Thakkar, N.; Gunthardt, C. E.; Masiello, D. J.; Gamelin, D. R. Charge-Tunable Quantum Plasmons in Colloidal Semiconductor Nanocrystals. *ACS Nano* **2014**, *8*, 1065−1072.

(5) Garcia, G.; Buonsanti, R.; Runnerstrom, E. L.; Mendelsberg, R. J.; Llordes, A.; Anders, A.; Richardson, T. J.; Milliron, D. J. Dynamically Modulating the Surface Plasmon Resonance of Doped Semiconductor Nanocrystals. *Nano Lett.* **2011**, *11*, 4415−4420.

(6) Hartstein, K. H.; Schimpf, A. M.; Salvador, M.; Gamelin, D. R. Cyclotron Splittings in the Plasmon Resonances of Electronically Doped Semiconductor Nanocrystals Probed by Magnetic Circular Dichroism Spectroscopy. *J. Phys. Chem. Lett.* **2017**, *8*, 1831−1836.

(7) Carroll, G. M.; Tsui, E. Y.; Brozek, C. K.; Gamelin, D. R. Spectroelectrochemical Measurement of Surface Electrostatic Contributions to Colloidal CdSe Nanocrystal Redox Potentials. *Chem. Mater.* **2016**, *28*, 7912−7918.

(8) Yalcin, S. E.; Labastide, J. A.; Sowle, D. L.; Barnes, M. D. Spectral Properties of Multiply Charged Semiconductor Quantum Dots. *Nano Lett.* **2011**, *11*, 4425−4430.

(9) Schimpf, A. M.; Gunthardt, C. E.; Rinehart, J. D.; Mayer, J. M.; Gamelin, D. R. Controlling Carrier Densities in Photochemically Reduced Colloidal ZnO Nanocrystals: Size Dependence and Role of the Hole Quencher. *J. Am. Chem. Soc.* **2013**, *135*, 16569−16577.

(10) Rinehart, J. D.; Schimpf, A. M.; Weaver, A. L.; Cohn, A. W.; Gamelin, D. R. Photochemical Electronic Doping of Colloidal CdSe Nanocrystals. *J. Am. Chem. Soc.* **2013**, *135*, 18782−18785.

(11) Koh, W.-k.; Koposov, A. Y.; Stewart, J. T.; Pal, B. N.; Robel, I.; Pietryga, J. M.; Klimov, V. I. Heavily Doped n-Type PbSe and PbS Nanocrystals using Ground-State Charge Transfer from Cobaltocene. *Sci. Rep.* [Online] **2013**, 3.10.1038/srep02004

(12) Liu, Z.; Beaulac, R. On the Nature of the Infrared Transition of Colloidal Indium Nitride Nanocrystals: Non-Parabolicity Effects on the Plasmonic Behavior of Doped Semiconductor Nanomaterials. *Chem. Mater.* **2017**, *29*, 7507−7514.

(13) Schimpf, A. M.; Lounis, S. D.; Runnerstrom, E. L.; Milliron, D. J.; Gamelin, D. R. Redox Chemistries and Plasmon Energies of Photodoped In_2O_3 and Sn-Doped In_2O_3 (ITO) Nanocrystals. *J. Am. Chem. Soc.* **2015**, *137*, 518−524.

(14) Brown, P. R.; Kim, D.; Lunt, R. R.; Zhao, N.; Bawendi, M. G.; Grossman, J. C.; Bulovic, V. Energy Level Modification in Lead Sulfide Quantum Dot Thin Films through Ligand Exchange. *ACS Nano* **2014**, *8*, 5863−5872.

(15) Chen, M.; Guyot-Sionnest, P. Reversible Electrochemistry of Mercury Chalcogenide Colloidal Quantum Dot Films. *ACS Nano* **2017**, *11*, 4165−4173.

(16) Carroll, G. M.; Schimpf, A. M.; Tsui, E. Y.; Gamelin, D. R. Redox Potentials of Colloidal n-Type ZnO Nanocrystals: Effects of

Confinement, Electron Density, and Fermi-Level Pinning by Aldehyde Hydrogenation. *J. Am. Chem. Soc.* **2015**, *137*, 11163−11169.

(17) Brozek, C. K.; Hartstein, K. H.; Gamelin, D. R. Potentiometric Titrations for Measuring the Capacitance of Colloidal Photodoped ZnO Nanocrystals. *J. Am. Chem. Soc.* **2016**, *138*, 10605−10610.

(18) Brus, L. E. A Simple Model for the Ionization Potential, Electron Affinity, and Aqueous Redox Potentials of Small Semiconductor Crystallites. *J. Chem. Phys.* **1983**, *79*, 5566−5571.

(19) Brus, L. E. Electron-Electron and Electron-Hole Interactions in Small Semiconductor Crystallites: The Size dependence of the Lowest Excited Electronic State. *J. Chem. Phys.* **1984**, *80*, 4403−4409.

(20) Goings, J. J.; Schimpf, A. M.; May, J. W.; Johns, R. W.; Gamelin, D. R.; Li, X. Theoretical Characterization of Conduction-Band Electrons in Photodoped and Aluminum-Doped Zinc Oxide (AZO) Quantum Dots. *J. Phys. Chem. C* **2014**, *118*, 26584−26590.

(21) Wang, L.-W.; Zunger, A. Pseudopotential Calculations of Nanoscale CdSe Quantum Dots. *Phys. Rev. B: Condens. Matter Mater. Phys.* **1996**, *53*, 9579−9582.

(22) Nienhaus, L.; Goings, J. J.; Nguyen, D.; Wieghold, S.; Lyding, J.; Li, X.; Gruebele, M. Imaging Excited Orbitals of Quantum Dots: Experiment and Electronic Structure Theory. *J. Am. Chem. Soc.* **2015**, *137*, 14743−14750.

(23) Gary, D. C.; Flowers, S. E.; Kaminsky, W.; Petrone, A.; Li, X.; Cossairt, B. M. Single-Crystal and Electronic Structure of a 1.3 nm Indium Phosphide Nanocluster. *J. Am. Chem. Soc.* **2016**, *138*, 1510−1513.

(24) Nelson, H. D.; Li, X.; Gamelin, D. R. Computational Studies of the Electronic Structures of Copper-Doped CdSe Nanocrystals: Oxidation States, Jahn-Teller Distortions, Vibronic Bandshapes, and Singlet-Triplet Splittings. *J. Phys. Chem. C* **2016**, *120*, 5714−5723.

(25) Chong, E. Q.; Lingerfelt, D. B.; Petrone, A.; Li, X. Classical or Quantum? A Computational Study of Small Ion Diffusion in II-VI Semiconductor Quantum Dots. *J. Phys. Chem. C* **2016**, *120*, 19434−19441.

(26) Light, J. C.; Carrington, T., Jr Discrete-Variable Representations and Their Utilization. *Adv. Chem. Phys.* **2000**, *114*, 263−310.

(27) Sharma, A. C. Size-Dependent Energy Band Gap and Dielectric Constant within the Generalized Penn Model Applied to a Semiconductor Nanocrystallite. *J. Appl. Phys.* **2006**, *100*, 084301.

(28) Mora-Sero, I.; Bertoluzzi, L.; Gonzalez-Pedro, V.; Gimenez, S.; Fabregat-Santiago, F.; Kemp, K. W.; Sargent, E. H.; Bisquert, J. Selective Contacts Drive Charge Extraction in Quantum Dot Solids via Asymmetry in Carrier Transfer Kinetics. *Nat. Commun.* [Online] **2013**, *4*.10.1038/ncomms3272

(29) Klein, A. Electronic Properties of In_2O_3 Surfaces. *Appl. Phys. Lett.* **2000**, *77*, 2009−2011.

(30) Frisch, M. J.; Trucks, G. W.; Schlegel, H. B.; Scuseria, G. E.; Robb, M. A.; Cheeseman, J. R.; Scalmani, G.; Barone, V.; Mennucci, B.; Petersson, G. A.; Nakatsuji, H.; Caricato, M.; Li, X.; Hratchian, H. P.; Izmaylov, A. F.; Bloino, J.; Zheng, G.; Sonnenberg, J. L.; Hada, M.; Ehara, M.; Toyota, K.; Fukuda, R.; Hasegawa, J.; Ishida, M.; Nakajima, T.; Honda, Y.; Kitao, O.; Nakai, H.; Vreven, T.; Montgomery, J. A., Jr.; Peralta, J. E.; Ogliaro, F.; Bearpark, M.; Heyd, J. J.; Brothers, E.; Kudin, K. N.; Staroverov, V. N.; Keith, T.; Kobayashi, R.; Normand, J.; Raghavachari, K.; Rendell, A.; Burant, J. C.; Iyengar, S. S.; Tomasi, J.; Cossi, M.; Rega, N.; Millam, J. M.; Klene, M.; Knox, J. E.; Cross, J. B.; Bakken, V.; Adamo, C.; Jaramillo, J.; Gomperts, R.; Stratmann, R. E.; Yazyev, O.; Austin, A. J.; Cammi, R.; Pomelli, C.; Ochterski, J. W.; Martin, R. L.; Morokuma, K.; Zakrzewski, V. G.; Voth, G. A.; Salvador, P.; Dannenberg, J. J.; Dapprich, S.; Parandekar, P. V.; Mayhall, N.; Daniels, A. D.; Farkas, O.; Foresman, J. B.; Ortiz, J. V.; Cioslowski, J.; Fox, D. J. *Gaussian Development Version*, revision H.21; Gaussian, Inc.: Wallingford, CT, 2012.

(31) Badaeva, E.; Feng, Y.; Gamelin, D. R.; Li, X. Investigation of Pure and Co^{2+}-Doped ZnO Quantum Dot Electronic Structures Using the Density Functional Theory: Choosing the Right Functional. *New J. Phys.* **2008**, *10*, 055013.

(32) Badaeva, E.; Isborn, C. M.; Feng, Y.; Ochsenbein, S. T.; Gamelin, D. R.; Li, X. Theoretical Characterization of Electronic Transitions in Co^{2+}- and Mn^{2+}-Doped ZnO Nanocrystals. *J. Phys. Chem. C* **2009**, *113*, 8710−8717.

(33) Adamo, C.; Barone, V. Toward Reliable Density Functional Methods Without Adjustable Parameters: The PBE0 Model. *J. Chem. Phys.* **1999**, *110*, 6158−6170.

(34) Perdew, J. P.; Burke, K.; Ernzerhof, M. Generalized Gradient Approximation Made Simple. *Phys. Rev. Lett.* **1996**, *77*, 3865−3868.

(35) Perdew, J. P.; Burke, K.; Ernzerhof, M. Generalized Gradient Approximation Made Simple [Phys. Rev. Lett. 77, 3865 (1996)]. *Phys. Rev. Lett.* **1997**, *78*, 1396−1396.

(36) Dunning, T. H., Jr.; Hay, P. J. In *Methods of electronic structure theory*; Schaefer, H. F., III, Ed.; Springer: New York, 1977; Vol. 3; pp 1−27.

(37) Wadt, W. R.; Hay, P. J. Ab initio Effective Core Potentials for Molecular Calculations. Potentials for Main Group Elements Na to Bi. *J. Chem. Phys.* **1985**, *82*, 284−298.

(38) Hay, P. J.; Wadt, W. R. Ab initio Effective Core Potentials for Molecular Calculations. Potentials for the Transition Metal Atoms Sc to Hg. *J. Chem. Phys.* **1985**, *82*, 270−283.

(39) Beaulac, R.; Feng, Y.; May, J. W.; Badaeva, E.; Gamelin, D. R.; Li, X. Orbital Pathways for Mn^{2+}-Carrier *sp*−*d* Exchange in Diluted Magnetic Semiconductor Quantum Dots. *Phys. Rev. B: Condens. Matter Mater. Phys.* [Online] **2011**, *84*.10.1103/PhysRevB.84.195324

(40) May, J. W.; McMorris, R. J.; Li, X. Ferromagnetism in p-Type Manganese-Doped Zinc Oxide Quantum Dots. *J. Phys. Chem. Lett.* **2012**, *3*, 1374−1380.

(41) May, J. W.; Ma, J.; Badaeva, E.; Li, X. Effect of Excited-State Structural Relaxation on Midgap Excitations in Co^{2+}-Doped ZnO Quantum Dots. *J. Phys. Chem. C* **2014**, *118*, 13152−13156.

(42) Peng, B.; May, J. W.; Gamelin, D. R.; Li, X. Effects of Crystallographic and Shape Anisotropies on Dopant-Carrier Exchange Interactions in Magnetic Semiconductor Quantum Dots. *J. Phys. Chem. C* **2014**, *118*, 7630−7636.

(43) Bradshaw, L. R.; May, J. W.; Dempsey, J. L.; Li, X.; Gamelin, D. R. Ferromagnetic Excited-State Mn^{2+} Dimers in $Zn_{1-x}Mn_xSe$ Quantum Dots Observed by Time-Resolved Magnetophotoluminescence. *Phys. Rev. B: Condens. Matter Mater. Phys.* [Online] **2014**, *89*.10.1103/PhysRevB.89.115312

(44) Lingerfelt, D. B.; Chong, E. Q.; Liu, H.; Li, X. Gauss-Hermite DVR Code.https://github.com/liresearchgroup/Gauss_Hermite_DVR. 2017

(45) Shockley, W. On the Surface States Associated with a Periodic Potential. *Phys. Rev.* **1939**, *56*, 317−323.

(46) Roest, A. L.; Kelly, J. J.; Vanmaekelbergh, D. Coulomb Blockade of Electron Transport in a ZnO Quantum-dot Solid. *Appl. Phys. Lett.* **2003**, *83*, 5530.

(47) Conway, B. E.; Bockris, J.; Ammar, I. A. The Dielectric Constant of the Solution in the Diffuse and Helmholtz Double Layers at a Charged Interface in Aqueous Solution. *Trans. Faraday Soc.* **1951**, *47*, 756−766.

(48) Jeong, K. S.; Deng, Z.; Keuleyan, S.; Liu, H.; Guyot-Sionnest, P. Air-Stable n-Doped Colloidal HgS Quantum Dots. *J. Phys. Chem. Lett.* **2014**, *5*, 1139−1143.